

Strain-tunable electronic and optical properties of h-BN/BC_3 heterostructure with enhanced electron mobility

Zhao-Yong Jiao(焦照勇), Yi-Ran Wang(王怡然), Yong-Liang Guo(郭永亮), and Shu-Hong Ma(马淑红),
Citation: Chin. Phys. B, 2021, 30 (**7**): 076801. DOI: 10.1088/1674-1056/abe29d
Journal homepage: http://cpb.iphy.ac.cn; http://iopscience.iop.org/cpb

What follows is a list of articles you may be interested in

Epitaxial fabrication of two-dimensional $TiTe_2$ monolayer on Au(111) substrate with Te as buffer layer

Zhipeng Song(宋志朋), Bao Lei(雷宝), Yun Cao(曹云), Jing Qi(戚竞), Hao Peng(彭浩), Qin Wang(汪琴), Li Huang(黄立), Hongliang Lu(路红亮), Xiao Lin(林晓), Ye-Liang Wang(王业亮), Shixuan Du(杜世萱), Hong-Jun Gao(高鸿钧)
Chin. Phys. B, 2019, 28 (**5**): 056801. DOI: 10.1088/1674-1056/28/5/056801

High quality $PdTe_2$ thin films grown by molecular beam epitaxy

En Li(李恩), Rui-Zi Zhang(张瑞梓), Hang Li(李航), Chen Liu(刘晨), Geng Li(李更), Jia-Ou Wang(王嘉鸥), Tian Qian(钱天), Hong Ding(丁洪), Yu-Yang Zhang(张余洋), Shi-Xuan Du(杜世萱), Xiao Lin(林晓), Hong-Jun Gao(高鸿钧)
Chin. Phys. B, 2018, 27 (**8**): 086804. DOI: 10.1088/1674-1056/27/8/086804

Growth and transport properties of topological insulator Bi_2Se_3 thin film on a ferromagnetic insulating substrate

Shanna Zhu(朱珊娜), Gang Shi(史刚), Peng Zhao(赵鹏), Dechao Meng(孟德超), Genhao Liang(梁根豪), Xiaofang Zhai(翟晓芳), Yalin Lu(陆亚林), Yongqing Li(李永庆), Lan Chen(陈岚), Kehui Wu(吴克辉)
Chin. Phys. B, 2018, 27 (**7**): 076801. DOI: 10.1088/1674-1056/27/7/076801

Effect of deposited temperatures of the buffer layer on the band offset of CZTS/In_2S_3 heterostructure and its solar cell performance

Jinling Yu(俞金玲), Zhongming Zheng(郑重明), Limei Dong(董丽美), Shuying Cheng(程树英), Yunfeng Lai(赖云锋), Qiao Zheng(郑巧), Haifang Zhou(周海芳), Hongjie Jia(贾宏杰), Hong Zhang(张红)
Chin. Phys. B, 2017, 26 (**4**): 046802. DOI: 10.1088/1674-1056/26/4/046802

Photodetecting and light-emitting devices based on two-dimensional materials

Yuanfang Yu(于远方), Feng Miao(缪峰), Jun He(何军), Zhenhua Ni(倪振华)
Chin. Phys. B, 2017, 26 (**3**): 036801. DOI: 10.1088/1674-1056/26/3/036801

Strain-tunable electronic and optical properties of h-BN/BC_3 heterostructure with enhanced electron mobility*

Zhao-Yong Jiao(焦照勇)[1], Yi-Ran Wang(王怡然)[1], Yong-Liang Guo(郭永亮)[1,2], and Shu-Hong Ma(马淑红)[1,†]

[1] *School of Physics, Henan Normal University, Xinxiang* 453007, *China*
[2] *School of Science, Henan Institute of Technology, Xinxiang* 453003, *China*

(Received 24 November 2020; revised manuscript received 15 January 2021; accepted manuscript online 3 February 2021)

By using first-principles calculation, we study the properties of h-BN/BC_3 heterostructure and the effects of external electric fields and strains on its electronic and optical properties. It is found that the semiconducting h-BN/BC_3 has good dynamical stability and ultrahigh stiffness, enhanced electron mobility, and well-preserved electronic band structure as the BC_3 monolayer. Meanwhile, its electronic band structure is slightly modified by an external electric field. In contrast, applying an external strain can mildly modulate the electronic band structure of h-BN/BC_3 and the optical property exhibits an apparent redshift under a compressive strain relative to the pristine one. These findings show that the h-BN/BC_3 hybrid can be designed as optoelectronic device with moderately strain-tunable electronic and optical properties.

Keywords: heterostructure, electronic and optical properties, first-principles calculation

PACS: 68.35.–p, 68.35.Gy, 68.65.–k **DOI:** 10.1088/1674-1056/abe29d

1. Introduction

Since the advent of graphene, atomically thin two-dimensional (2D) layered materials, such as insulating hexagonal boron nitride (h-BN), semiconducting molybdenum disulfide (MoS_2), and conducting MXenes, have triggered world interest due to their superior properties[1,2] and the possibility of combining diverse atomic layers to create mechanically stacked heterostructures for manufacturing high-performance devices.[3–9]

Owing to the atomically flat and inert surface, h-BN monolayer has proven to be beneficial to a variety of multifunctional devices consisting of graphene,[10–13] MoS_2,[14–17] and others.[18–20] For example, the use of h-BN thin film as a substrate for monolayer MoS_2 can reduce the Coulombic charge scattering, lower the Schottky barrier height, and enhance the carrier mobility, showing excellent performance for optoelectronic device.[5,14,17,21] This has also been evidenced on another Gr/h-BN/$MoSe_2$ heterostructure by vertically stacking graphene (Gr) on the top of 2D h-BN and $MoSe_2$.[3,22]

Likewise, the semiconducting BC_3 monolayer, mimicking graphene in geometrical structure, has shown distinctive features such as a high elastic moduli ($\sim$ 256 N/m), an excellent thermal conductivity ($\sim$ 410 W/mK), a relatively high carrier mobility of hole (5.13×10^4 $cm^2\cdot V^{-1}\cdot s^{-1}$ along the armchair direction), a favorable optical response to visible light,[23,24] and a strain-tunable electronic and optical properties,[23–26] improved optical responses via combining with C_3N monolayer forming heterostructure,[27] which make it appealing to optoelectronic device design. Besides, the controllable properties via using an electric-field/strain have been predicted in a number of other van der Waals (vdW) heterostructures.[4,27–30]

It is thus intriguing to make clear what the properties of the heterostructure vertically stacked by BC_3 and h-BN monolayers are, and how the heterostructure responds to an applied external electric field and strain. In this work, we study the feasibility of forming 2D heterostructure of h-BN/BC_3, focusing on its stability, mechanical property, carrier mobility, electronic and optical properties, by performing first-principles calculation. Moreover, the electronic band structure of h-BN/BC_3 is evaluated under an applied electric field and external strain, and the optical properties are investigated as well.

2. Computational details

First-principles calculation was performed within the density functional theory (DFT) framework by using projector-augmented wave (PAW) pseudopotential, as implemented in VASP code,[31] in conjunction with the generalized gradient approximation (GGA) of the Perdew–Burke–Ernzerhof (PBE) functional.[32] A plane wave basis set with a kinetic energy cutoff of 500 eV and the van der Waals (vdW) interaction with the DFT-D2 correction[33] were considered in the calculations. The optimized structures were obtained by relaxing all atomic positions through using the conjugate gradient scheme until the energy and force converged to 10^{-5} eV and 0.01 eV/Å, respectively.

*Project supported by the National Natural Science Foundation of China (Grant No. 11904081) and the Natural Science Foundation of Henan Province, China (Grant Nos. 202300410247 and 21A140013).

†Corresponding author. E-mail: mash.phy@htu.edu.cn

© 2021 Chinese Physical Society and IOP Publishing Ltd

The optimized lattice parameters of freestanding h-BN and BC_3 monolayer were 2.51 Å and 5.17 Å, respectively, which together with the interatomic bond lengths are shown in Fig. 1(a). Figure 1(a) also shows the comparison between our results and previous results in the literature.[22,25] The unit cell of the h-BN/BC_3 heterostructure with a small lattice mismatch of about 2.9%, was prepared with different stacking patterns by using a 2×2 supercell of h-BN monolayer and a primitive cell of BC_3 monolayer (see Figs. 1(b)–1(e)), consisting of six boron atoms, six carbon atoms, and four nitrogen atoms, and a vacuum layer of 16 Å. The Brillouin zone[34] was sampled with $7\times7\times1$ and $11\times11\times1$ k-points for structural relaxation and electronic property calculations, respectively, and the charge transfers were obtained by the Bader charge method.[35]

3. Results and discussion

3.1. Equilibrium geometrical structure and stability

Firstly, the stability of heterostructure is evaluated by the interface formation energy ($E_{\rm form}$) defined as $E_{\rm form} = E^{\rm total}_{\rm h-BN/BC_3} - E^{\rm total}_{\rm h-BN} - E^{\rm total}_{\rm BC_3}$, where $E^{\rm total}_{\rm h-BN/BC_3}$, $E^{\rm total}_{\rm h-BN}$ and $E^{\rm total}_{\rm BC_3}$ represent the total energy of h-BN/BC_3 heterostructure and its separate freestanding monolayers, respectively. The obtained formation energies are −0.28, −0.25, −0.25, and −0.15 eV for the four heterojunction configurations denoted as S_1, S_2, S_3, and S_4 in Fig. 1, respectively with the almost identical interlayer spacing of 3.15, 3.13, 3.19, and 3.15 Å. Thus, the most stable configuration S_1 is taken as an representative as follows, unless otherwise stated. As displayed in Figs. 1(a) and 1(b), the geometrical structure of S_1 has the interatomic bond length of C–C (1.41 Å), C–B (1.54 Å), and B–N (1.47 Å), exhibiting tiny changes compared with its single component.

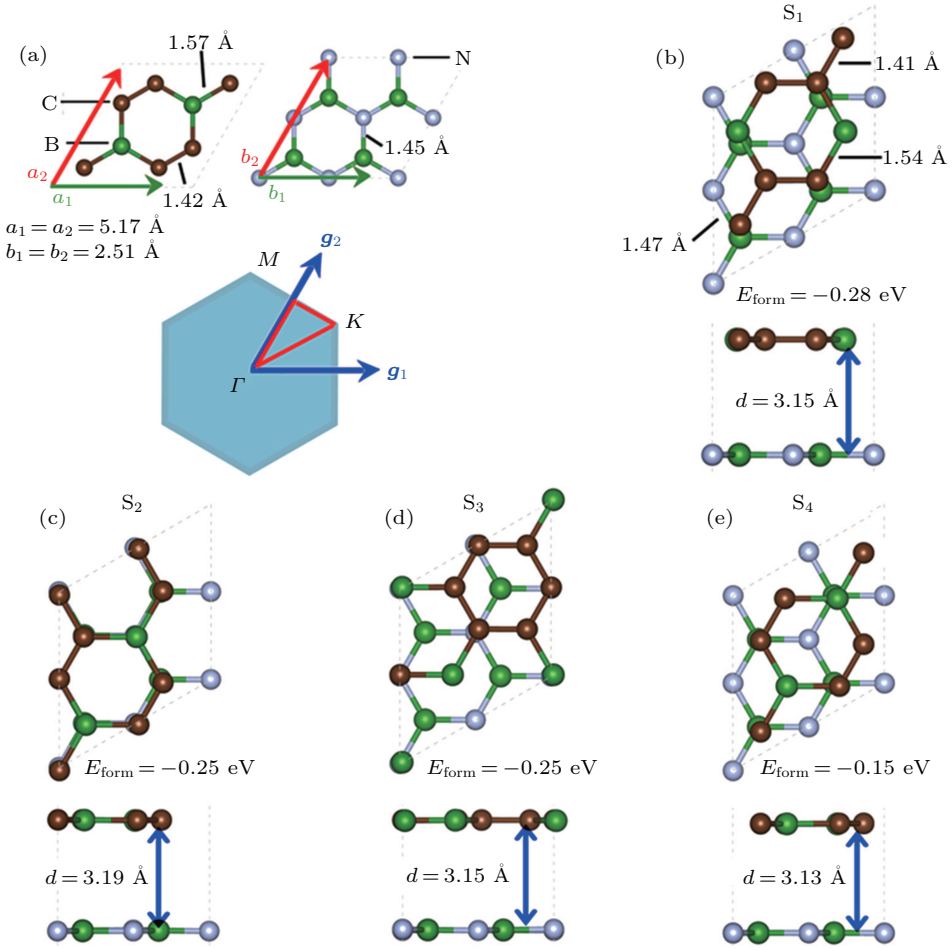


Fig. 1. (a) Top views of h-BN and BC_3 primitive unit cells with their lattice parameters (a_1, a_2) and (b_1, b_2), and hexagonal Brillouin zone and three high-symmetry points, Γ, M, and K in reciprocal space with basis vectors $\boldsymbol{g}_1$ and $\boldsymbol{g}_2$. (b)–(e)) Top and side views for optimized configurations of h-BN/BC_3 heterostructure. Corresponding bond distances, interlayer distances, and formation energies are also shown.

Meanwhile, the most favorable configuration S_1 is also determined by the increased energy (ΔE) relative to the equilibrium configuration of h-BN/BC_3 as indicated in Fig. 2(a), which are obtained by examining the lateral displacements of the h-BN monolayer along the in-plane x and y directions (δ_{xy}) in the h-BN/BC_3 interface, respectively. In the case of configuration S_1, the binding energy ($E_{\rm bind}$) defined by $E_{\rm bind} = (E^{\rm total}_{\rm h-BN} - E^{\rm total}_{\rm h-BN+BC_3})/S$, where $E^{\rm total}_{\rm h-BN+BC_3}$ denotes the sum of the total energy of freestanding h-BN and BC_3 monolayer fixed in their corresponding heterostructure

lattice, S is the sectional area of h-BN/BC_3, the E_{bind} is estimated to be -22.04 meV/Å^2, quite close to the C_3N/graphene (-20.72 meV/Å^2).[36] Besides, the excellent structural stability of configuration S_1 is shown in Fig. 2(b) by varying its binding energy with vertical interlayer spacing (d) between the h-BN sheet and BC_3 sheet. In the equilibrium geometry, the vertical interlayer distance $d = 3.15$ Å implies the absence of chemical bonds between the h-BN and BC_3 sheets, thus confirming the vdW interaction at the h-BN/BC_3 interface.

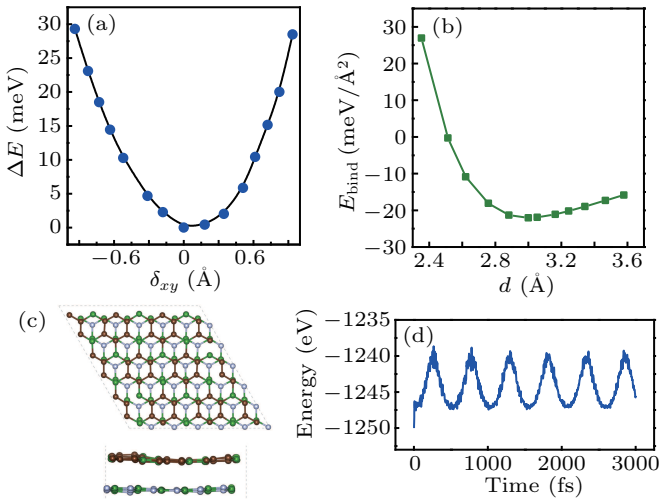


Fig. 2. (a) Evolution of total energy difference with displacement δ_{xy} of the BC_3 layer relative to h-BN, with origin taken at the lowest energy configuration. (b) Binding energy per unit cell *versus* interlayer spacing d of h-BN/BC_3 heterostructure. [(c), (d)] Molecular dynamics simulations for final structural configuration after 3000 fs and total energy fluctuations with time for h-BN/BC_3 at $T = 300$ K, respectively.

Additionally, the good thermal stability of h-BN/BC_3 heterostructure at 300 K is verified by the slight energy fluctuation in a period of 3 ps in time steps of 1 fs and the well-retained final structure shown in Figs. 2(c) and 2(d), obtained by performing the *ab initio* molecular dynamics (AIMD) simulations with the constant particle number–volume–temperature (NVT) canonical ensemble.[37] All the features manifest a stable equilibrium geometry of configuration S1 for the vdW h-BN/BC_3 heterostructure.

3.2. Mechanical properties

To ascertain the mechanical stability, the elastic properties of h-BN/BC_3 heterostructure are determined in comparison with those of its free-standing components. For the 2D hexagonal phase structure, the elastic constants (C_{xx} and C_{yy}) reveal the material's stiffness response to uniaxial tensile strain in the armchair (x) direction and zigzag (y) direction,[36] respectively, while C_{xy} represents the resistance of the material to the in-plane biaxial tensile strain. The Young's modulus[38] $Y^{2D}_{x(y)} = (C_{xx}C_{yy} - C^2_{xy})/C_{yy(xx)}$ and Poisson's ratio $\nu^{2D}_{x(y)} = C_{xy}/C_{yy(xx)}$ represent the ability of material to resist the deformation and the extent of deformation of material, respectively.

According to the calculations in Table 1, the four independent elastic constants: C_{11}, C_{22}, C_{12}, and C_{44} (1.18 N/m) and the others fit well with Born's mechanical stability criteria:[41] $C_{44} > 0$, $C_{11} > |C_{12}|$, and $(C_{11} + 2C_{22})C_{33} > 2C^2_{13}$, displaying a good mechanical stability of the h-BN/BC_3 heterostructure. Moreover, the nearly identical elastic constants ($C_{11(22)}$), the Young's moduli, and the Poisson's ratios along different directions show an isotropic behavior of the h-BN/BC_3 heterostructure, as well as similar compressibility, stretchability to its components due to the quite similar elastic constants. In contrast, the stiffness of the h-BN/BC_3 nanohybrid is greatly improved by nearly twice larger in elastic constants ($C_{11} = 583.454$ N/m and $C_{22} = 580.59$ N/m) and the Young's moduli than its two isolated components. In comparison with the C_3N/graphene heterostructure,[36] the h-BN/BC_3 is predicted to have a slightly less stiffness and a quite close Poisson's ratio.

Table 1. Calculated elastic constants $C_{xx(yy/xy)}$ (N/m) ($x = 1$, $y = 2$), Young's modulus $Y^{2D}_{x(y)}$ (N/m), and Poisson's ratio $\nu^{2D}_{x(y)}$ for h-BN/BC_3 nanohybrid in comparison with those of monolayer h-BN, BC_3 and graphene.

System	C_{xx}	C_{yy}	C_{xy}	$Y^{2D}_{x(y)}$	$\nu^{2D}_{x(y)}$	
h-BN/BC_3	583.45	580.59	100.2	566.16 (563.38)	0.17 (0.17)	this work
h-BN	288.12	288.12	60.38	275.33	0.21	this work
	267	267				Ref. [39]
BC_3	289.54	289.54	43.35	283.01	0.15	this work
	316.2	316.2	/	/	/	Ref. [23]
Graphene	354.7	354.7	59.3	345	0.167	Ref. [36]
	339			321	0.230	Ref. [40]
C_3N	359.7	359.7	56.6	351	0.157	Ref. [36]

3.3. Electronic properties

To gain more knowledge of the h-BN/BC_3 heterostructure, we calculate the electronic properties such as the electrostatic potential, electron charge redistribution and electronic band alignment. As shown in Fig. 3(a), the electrostatic-potential-well depths of its two isolated components are almost identical, giving rise to a rather weak electron charge redistribution occurring in the vdW gap. This is in good accordance with the plot of the three-dimensional (3D) charge density difference (CDD) and plot of the xy-plane average CDD *versus* z shown in Fig. 3(b). A small number of 0.02 electrons

are predicted to flow from h-BN side to BC_3 sheet. It is notable that all the band structures are calculated at GGA-PBE level and the obtained band-gaps are 4.65 eV and 0.67 eV for the freestanding h-BN and BC_3 sheet, respectively, which are in good agreement with other calculations.[27] In Fig. 3(c), the projected band structures on h-BN (black dots) and BC_3 (red dots) monolayer display that the electronic states of h-BN in the h-BN/BC_3 composite are far from the Fermi level and that the electronic states of BC_3 monolayer are preserved as well as those of single-layer BC_3. In other words, neither the conduction band minimum (CBM) nor the valence band maximum (VBM) of h-BN/BC_3 is disturbed by h-BN. The band-gap of h-BN/BC_3 gets narrower slightly down to 0.56 eV at PBE level (1.70 eV at HSE06 level) relative to that of monolayer BC_3 (0.67 eV at PBE level). Like h-BN/InSe,[42] the h-BN/BC_3 heterojunction exhibits type-I band alignment (see Fig. 3(d)) due to the large band-gap discrepancy between the h-BN and BC_3, which is useful for light-emitting diodes (LEDs) and optoelectronic devices requiring a quantum well structure. Meanwhile, the work function (Φ) defined by $\Phi = E_{\rm vac} - E_{\rm F}$, with $E_{\rm vac}$ and $E_{\rm F}$ denoting the vacuum level and Fermi level, respectively, is obtained to be 5.21 eV for h-BN/BC_3, which is between those of monolayer h-BN (6.19 eV) and monolayer BC_3 (4.85 eV). All these characteristics show a weaker vdW interaction on forming the h-BN/BC_3 heterostructure and its electronic structure is mainly predominated by monolayer BC_3.

Further considering a heterostructure as an electronic device, we evaluate the electronic band structure of h-BN/BC_3 heterostructure under external electric field (E-field). As shown in Fig. 4, the applied E-field has a slight effect on the electronic band structure, which retains an indirect semiconducting band. For instance, the tiny upshift (less than 0.1 eV) of the conductive band minimum, combining with a nearly constant valence band maximum, gives rise to the band-gap ranging from 0.51 eV to 0.61 eV under an E-field. What is notable is that the valence band edge at K point moves downward with the positive E-field increasing, while under the action of a negative E-field it shifts to higher energy and this upshift becomes more prominent with E-field turns more negative, finally the VBM moves away from Γ to K point under an E-field strength of -0.5 V/Å, quite approaching to the Fermi level ($E_{\rm F}$). Meanwhile, the further increasing of negative E-field strength can narrow the band-gap to 0.28 eV under an E-field strength of -0.7 V/Å, by downshifting the CBM. Overall, the electronic band structure of h-BN/BC_3 heterostructure exhibits a slight variation under the applied E-field with its strength less than 0.5 V/Å.

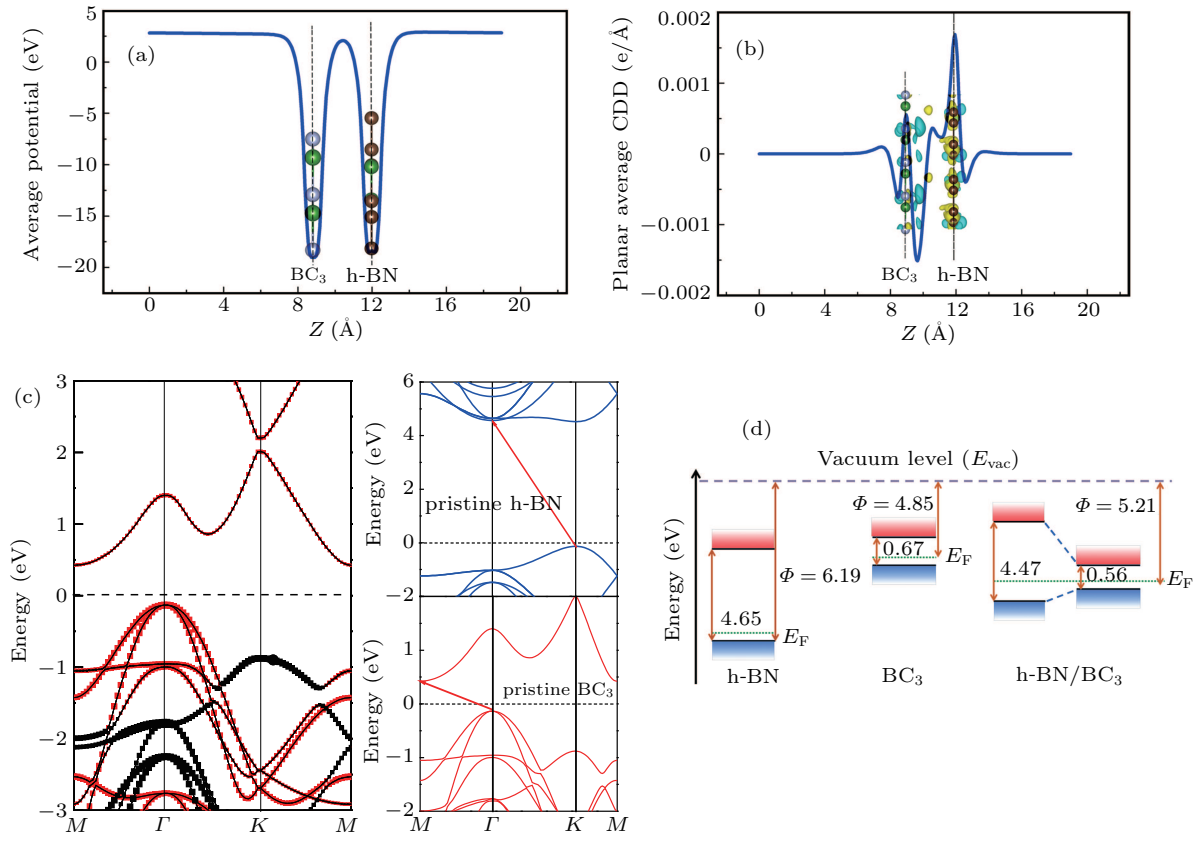


Fig. 3. (a) Average electrostatic potential of h-BN/BC_3 heterostructure *versus* z. (b) Planar average charge density difference (CDD) *versus* z of heterostructure, with insert showing 3D isosurface of CDD and the cyan/yellow region representing electron depletion/accumulation with an isosurface value of 0.0004 e/Å^3. (c) Band structures (at PBE level) of monolayer h-BN, monolayer BC_3, and h-BN/BC_3 heterostructures, with Fermi level ($E_{\rm F}$) set to be zero. Contributions of BC_3 and h-BN to the projected band structure are represented in red and black, respectively. (d) Band alignments of monolayer h-BN, monolayer BC_3, and h-BN/BC_3 heterostructures with respect to the vacuum level.

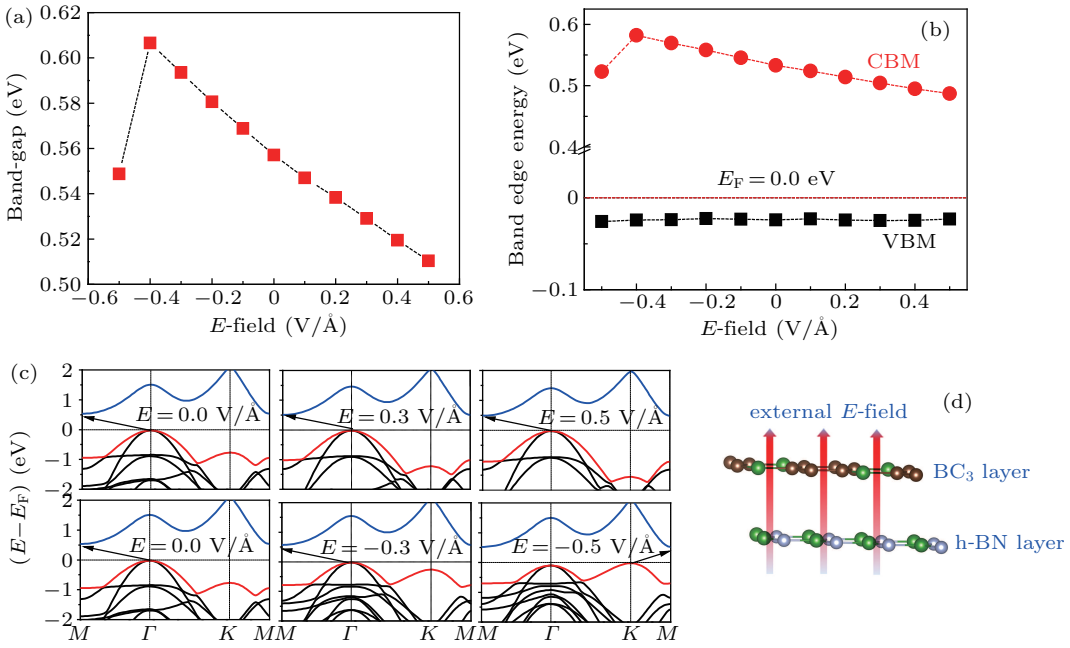


Fig. 4. Variation of (a) band-gap, (b) band-edge, and (c) electronic band structures of h-BN/BC_3 heterostructure with external electric fields (E-field). (d) E_F being set to be zero and applied E-field being defined, with the arrow indicating the forward direction.

3.4. In-plane strain effect on heterostructure

3.4.1. Carrier mobility under uniaxial strains

As is well known, carrier mobility plays a crucial role in evaluating the electrical properties of semiconductor materials.[43–45] According to deformation potential (DP) theory, the carrier mobilities of many typical nanomaterials can be predicted successfully with the formula: $\mu = 2e\hbar^3 C/3k_B T|m^*|^2 E_1^2$, where m^* is the effective mass, T is the temperature, and C is the elastic modulus and can be calculated from $C = [\partial^2 E/\partial\delta^2]/S^0$, with E, δ, and S^0 denoting the total energy of the supercell, the applied uniaxial strain, and the area of the optimized structure. The DP constant E_1 is relevant to the energy shift of the band edge (ΔE), defined by $\Delta E = E_1(\Delta l/l)$, where $\Delta l/l$ represents the lattice dilation along the zigzag and armchair direction.

As displayed in Fig. 5(a), the orthogonal supercell of h-BN/BC_3 is used to calculate the carrier mobilities along the x

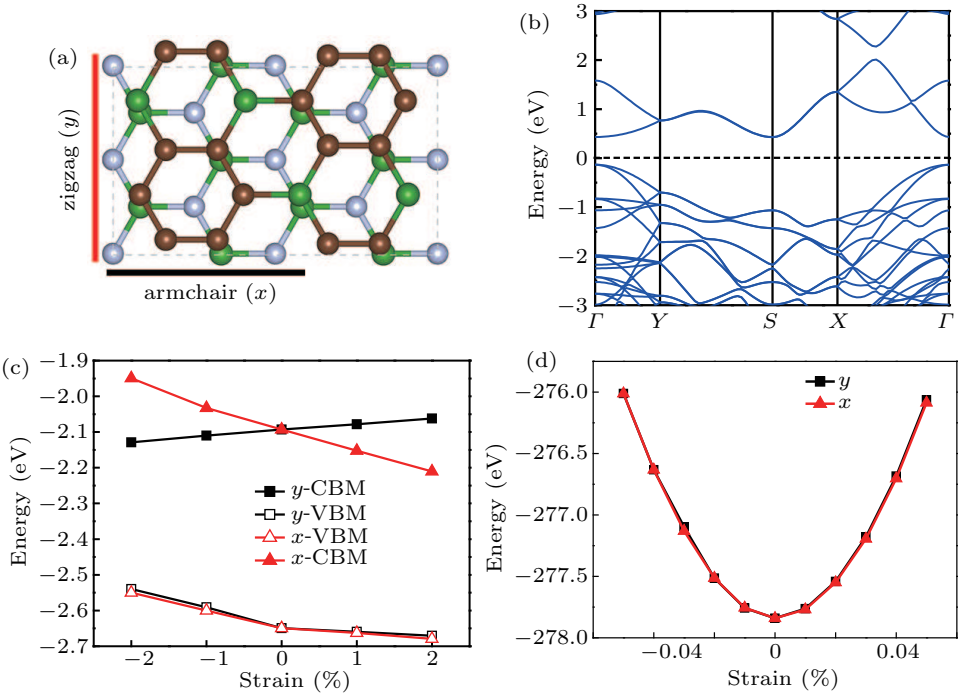


Fig. 5. (a) Orthogonal supercell of h-BN/BC_3 heterostructure, (b) band structure of h-BN/BC_3 heterostructure, (c) band energies of the VBMs and CBMs *versus* uniaxial strain along armchair and zigzag direction for h-BN/BC_3, and (d) total energy with respect to uniaxial strain relationship along x direction and y direction of h-BN/BC_3.

Table 2. Calculated deformation potential constant E_1, in-plane stiffness C, effective mass m^*, and electron and hole mobility μ in x direction and y direction of h-BN/BC_3 heterostructure at 300 K.

System	Carrier type	E_1 (eV)	C (N/m)	m^* (m_e)	μ (10^3 cm^2·V^{-1}·s^{-1})	
h-BN/BC_3	e (x)	–7.28	583.45	0.18	4.86	this work
	h (x)	–0.80	583.45	0.90	16.09	
	e (y)	1.66	580.59	1.68	1.07	
	h (y)	–1.35	580.59	0.72	8.79	
BC_3	e (x)	–5.43	289.54	1.37	0.08	this work
	h (x)	–5.89	289.54	0.88	0.16	
	e (y)	3.00	289.54	0.17	16.85	
	h (y)	–5.53	289.54	0.74	0.25	
BC_3	e (x)	3.80	295.98	1.18	0.21	Ref. [26]
	h (x)	9.54	295.98	0.03	51.30	
	e (y)	5.04	303.01	1.26	0.11	
	h (y)	4.84	303.01	0.66	0.42	

direction and y direction, and the related results are given in Table 2. Firstly, the effective mass in h-BN/BC_3 is predicted to be $0.18m_e$ for electrons and $0.90m_e$ for holes along the x direction, $1.68m_e$ for electrons and $0.72m_e$ for holes along the y direction in our studies. As for other two elements related to the carrier mobility, the DP constant E_1 is a parameter of the coupling strength of electron or hole to the acoustic phonon, which can be calculated by linearly fitting the data of compressing and stretching the lattice constants along the x direction and y direction in Fig. 5(d). Meanwhile, the mobile carries of monolayer BC_3 are listed in Table 2, which have a slight difference with previous calculations,[26] the possibility may be the PBE functional considered in our calculation while HSE06 functional employed in the work of Zhang *et al*. It can be seen that the calculated values of E_1 along the x/y direction for hole/electron in Table 2 for h-BN/BC_3 are different from those for the monolayer BC_3. In particular, for the h-BN/BC_3 the absolute value of E_1 along the x direction for electron is nearly doubled and inversely, that of hole along the same direction is considerably lowered to 0.80. And the elastic modulus C is estimated at 583.45 N/m and 580.59 N/m along the x direction and y direction for h-BN/BC_3, nearly twice as much as that of monolayer BC_3.[26] Comparing with BC_3 monolayer, the enhanced mobile carries in h-BN/BC_3 correspond to the narrower band-gap.

Based on the above calculations, the carrier mobilities of h-BN/BC_3 at room temperature (300 K) are given in Table 2, which shows an anisotropic behavior and is nearly ten times larger than that of monolayer BC_3, except for the lowered hole mobility along the x direction. The obtained mobility for electrons is 4.86×10^3 cm^2·V^{-1}·s^{-1} and 1.07×10^3 cm^2·V^{-1}·s^{-1} along the x direction and y direction, respectively, while that for holes along the x direction goes up to 16.09×10^3 cm^2·V^{-1}·s^{-1}, twice as large as that along the y direction. The enhanced carrier mobility is quite vital for high-performance optoelectronic devices.

3.4.2. Electronic and optical properties under biaxial strains

A number of previous theoretical and experiment research studies show that the use of external strain is an effective method to modulate the electronic and optical properties of the 2D materials.[25,46] Hence, we also examine the effect of in-plane biaxial strain ($\varepsilon_{\parallel}$) ranging from -6% to 6% as proposed previously[25] on the electronic and optical properties of h-BN/BC_3, with the definition $\varepsilon_{\parallel}=(l-l_0)/l_0$, with l and l_0 corresponding to the lattice constant with and without strain. At zero strain, a band-gap of 1.70 eV obtained at HSE06 level enable the h-BN/BC_3 heterostructure to be a promising photocatalyst with a visible-light absorption. Like the bilayer BC_3,[25] an external strain is used to modify the electronic band structure of h-BN/BC_3, *i.e*., band-gap expands with the tensile strain increasing due to an upshift of CBM at a high symmetry M point together with the almost unchanged VBM at Γ point, and an inverse case under the compressive strains as shown in Fig. 6(a). A nearly linear increase of the band-gap with strain varying from -6% to 6% is observed from Fig. 6(b), except for a slight deviation under a compressive strain of 4%. Thus, it is feasible to moderately modulate the band gap of h-BN/BC_3 via applying an external strain. To evaluate the thermal stability, *ab initio* molecular dynamics (AIMD) simulations are conducted for h-BN/BC_3 under 6% and -6% strains at 300 K. Figure 7 shows that the energy oscillates within a small range for h-BN/BC_3 during the period of AIMD simulation, and the final relaxed configuration has a slight deformation compared with the initial structure. Hence, it is confirmed that the h-BN/BC_3 possesses good stability under strain.

The optical absorption properties are further evaluated by the complex dielectric function $\varepsilon(\omega)=\varepsilon_1(\omega)+\mathrm{i}\varepsilon_2(\omega)$. The imaginary part $\varepsilon_2(\omega)$ is obtained from the electronic structures by using the joint density of states and the optical matrix overlap, and the real part $\varepsilon_1(\omega)$ follows the Kramers–Kroning relationship. The obtained dielectric constants (see Fig. 6(c)) show an optical gap of 2.05 eV for h-BN/BC_3, confirming

the visible-light absorption. Meanwhile, one can observe an enhanced intensity of peak and a prominent red shift in the imaginary part of dielectric function spectrum for h-BN/BC_3 under zero strain as compared with those for BC_3 monolayer. Especially, there are two absorption regions for h-BN/BC_3, *i.e.*, the high absorption region from 1.5 eV to 5.0 eV, and the low absorption region between 5.0 eV and 10.0 eV. The large area under the ε_2 curve in the visible-light region from 1.5 eV to 5.0 eV with the highest peak of absorption spectrum at 2.73 eV, implies a high efficiency visible-light absorption and high absorption coefficient at these frequencies for h-BN/BC_3. Additionally, under an applied tensile strain this heterostructure shows an optical response quite similar to pristine h-BN/BC_3. In contrast, the applying of compressive strain (*i.e.*, −6%) can redshift the optical spectrum, with band-gap reducing 0.68 eV, and the peak intensity lowering about 3.80 eV.

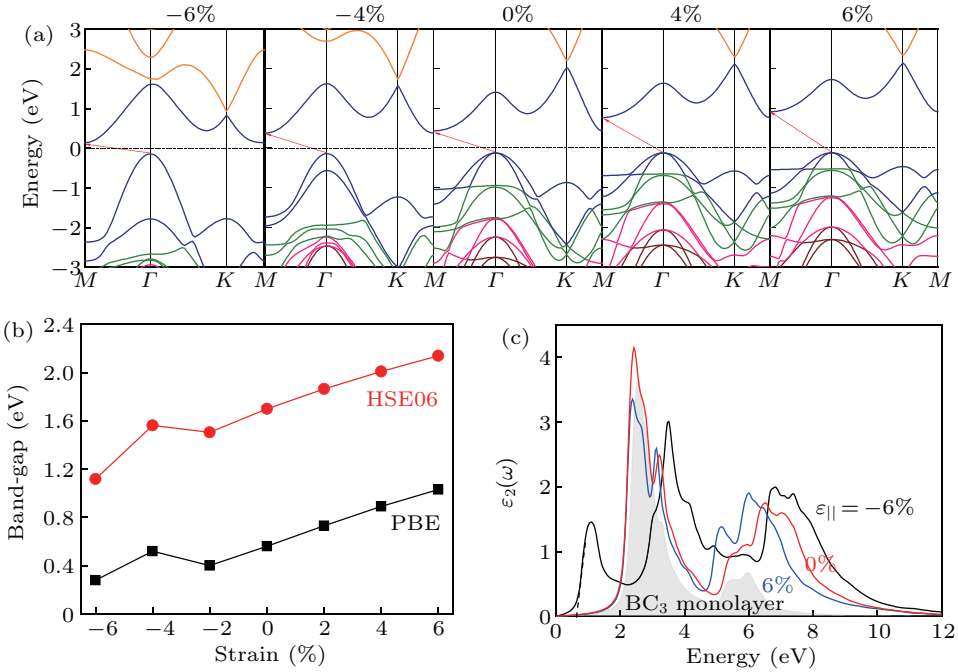


Fig. 6. Calculated results for h-BN/BC_3 heterostructure under applied in-plane biaxial strain ($\varepsilon_{||}$). (a) Electronic band structure (at PBE level), (b) band-gap (at PBE/HSE06 level), and (c) imaginary part of dielectric function.

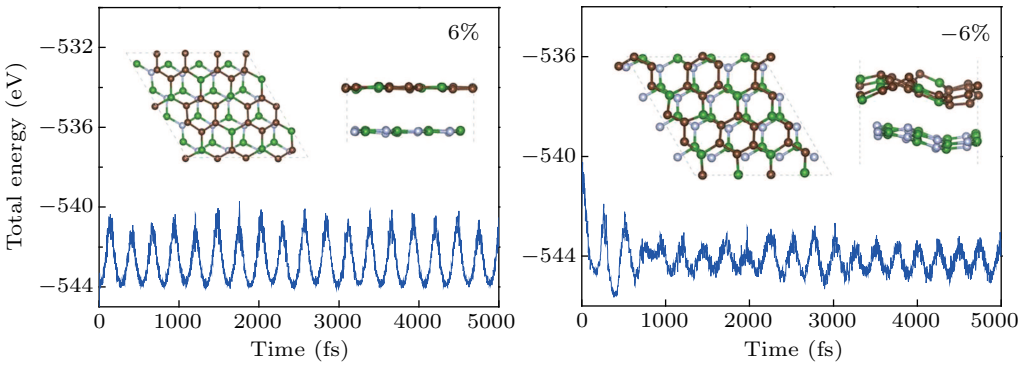


Fig. 7. Variations of energy with AIMD simulation time for h-BN/BC_3 heterostructure under 6% and −6% strains with simulation lasting 5 ps at 300 K. And resulting structure is in the middle of the image.

4. Conclusions

By using first-principles calculation, we have studied the structural, mechanical and electronic properties of the h-BN/BC_3 heterostructure. The results indicate that the electronic properties of BC_3 monolayer are well preserved and the electron mobilities are enhanced by around ten times in the ultrahigh stiff van der Waals heterostructure. Moreover, the applying of an external electric field only induces its electronic band structure to be modified slightly, while an applied external strain can manipulate the electronic and optical properties of h-BN/BC_3, especially under compressive strain. These findings manifest that the h-BN/BC_3 heterostructure can be used in BC_3-based optoelectronic devices.

References

[1] Schleder G R, Acosta C M and Fazzio A 2020 *ACS Appl. Mater. Inter.* **12** 20149

[2] Jiang X, Kuklin A V, Baev A, Ge Y, Ågren H, Zhang H and Prasad P N 2020 *Phys. Rep.* **848** 1
[3] Cheng R, Wang F, Yin L, Xu K, Ahmed Shifa T, Wen Y, Zhan X, Li J, Jiang C, Wang Z and He J 2017 *Appl. Phys. Lett.* **110** 173507
[4] Zhao J, Zeng H and Zhou X 2019 *Carbon* **145** 1
[5] Joo M K, Moon B H, Ji H, Han G H, Kim H, Lee G, Lim S C, Suh D and Lee Y H 2016 *Nano Lett.* **16** 6383
[6] Kim K K, Lee H S and Lee Y H 2018 *Chem. Soc. Rev.* **47** 6342
[7] Wang W, Lei W, Zhang X J, Li H, Tang X and Ming X 2020 *Chin. Phys. B* **29** 056201
[8] Ma X, Zhang R, An C, Wu S, Hu X and Liu J 2019 *Chin. Phys. B* **28** 037803
[9] Aeschlimann S, Rossi A, Chávez-Cervantes M, Krause R, Arnoldi B, Stadtmüller B, Aeschlimann M, Forti S, Fabbri F, Coletti C and Gierz I 2020 *Sci. Adv.* **6** 0761
[10] Sajjad M, Makarov V, Mendoza F, Sultan M S, Aldalbahi A, Feng P X, Jadwisienczak W M, Weiner B R and Morell G 2019 *Nanomaterials* **9** 925
[11] Chen X K, Pang M, Chen T, Du D and Chen K Q 2020 *ACS Appl. Mater. Inter.* **12** 15517
[12] Iwasaki T, Endo K, Watanabe E, Tsuya D, Morita Y, Nakaharai S, Noguchi Y, Wakayama Y, Watanabe K, Taniguchi T and Moriyama S 2020 *ACS Appl. Mater. Inter.* **12** 8533
[13] De Sanctis A, Mehew J D, Alkhalifa S, Withers F, Craciun M F and Russo S 2018 *Nano Lett.* **18** 7919
[14] Wang J, Yao Q, Huang C W, Zou X, Liao L, Chen S, Fan Z, Zhang K, Wu W, Xiao X, Jiang C and Wu W W 2016 *Adv. Mater.* **28** 8302
[15] Su J, Feng L P, Zheng X, Hu C, Lu H and Liu Z 2017 *ACS Appl. Mater. Inter.* **9** 40940
[16] Pande G, Siao J Y, Chen W L, Lee C J, Sankar R, Chang Y M, Chen C D, Chang W H, Chou F C and Lin M T 2020 *ACS Appl. Mater. Inter.* **12** 18667
[17] Liu B, Zhao Y Q, Yu Z L, Wang L Z and Cai M Q 2018 *J. Colloid Interface Sci.* **513** 677
[18] Afzal A M, Javed Y, Akhtar Shad N, Iqbal M Z, Dastgeer G, Munir Sajid M and Mumtaz S 2020 *Nanoscale* **12** 3455
[19] Li Q, Liu M, Zhang Y and Liu Z 2016 *Small* **12** 32
[20] Guo Q, Wang G, Kumar A and Pandey R 2017 *Nanotechnology* **28** 475708
[21] Gwan-Hyoung Lee, Cui X, Kim Y D, Arefe G, Zhang X, Lee C H, Ye F, Watanabe K, Taniguchi T, Kim P and Hone J 2015 *ACS Nano* **9** 7019
[22] Pham K D and Nguyen C V 2018 *Diam. Relat. Mater.* **88** 151
[23] Zhang Y, Wu Z F, Gao P F, Fang D Q, Zhang E H and Zhang S L 2018 *RSC Adv.* **8** 1686
[24] Mortazavi B, Shahrokhi M, Raeisi M, Zhuang X, Pereira L F C and Rabczuk T 2019 *Carbon* **149** 733
[25] Behzad S 2017 *Surf. Sci.* **665** 37
[26] Zhang H, Liao Y, Yang G and Zhou X 2018 *ACS Omega* **3** 10517
[27] Luo M, Xu Y E and Zhang Q X 2018 *Solid State Comm.* **273** 44
[28] Yuan P F, Han J N, Fan Z Q, Zhang Z H and Wang C Z 2020 *J. Phys.: Condens. Matter.* **32** 475001
[29] Xie Z, Sun F, Yao R, Zhang Y, Zhang Y, Zhang Z, Fan J, Ni L and Duan L 2019 *Appl. Surf. Sci.* **475** 839
[30] Zeng H, Zhao J, Cheng A Q, Zhang L, He Z and Chen R S 2018 *Nanotechnology* **29** 075201
[31] Kresse G and Furthmüller J 1996 *Phys. Rev. B* **54** 11169
[32] Kresse G and Joubert D 1999 *Phys. Rev. B* **59** 1758
[33] Grimme S 2006 *J. Comput. Chem.* **27** 1787
[34] Monkhorst H J 1977 *Phys. Rev. B* **16** 1748
[35] Henkelman G, Arnaldsson A and Jónsson H 2006 *Comput. Mater. Sci.* **36** 354
[36] Wang Y R, Jiao Z Y, Ma S H and Guo Y L 2019 *J. Power Sour.* **413** 117
[37] Sánchez-Monroy X, Torres-Arenas J and Gil-Villegas A 2019 *J. Chem. Phys.* **150** 144507
[38] Zhao T, Zhang S, Guo Y and Wang Q 2016 *Nanoscale* **8** 233
[39] ahin H, Cahangirov S, Topsakal M, Bekaroglu E, Akturk E, Senger R T and Ciraci S 2009 *Phys. Rev. B* **80** 155453
[40] Fu Z H, Zhang Q F, Legut D, Si C, Germann T C, Lookman T, Du S Y, Francisco J S and Zhang R F 2016 *Phys. Rev. B* **94** 104103
[41] Wu Z J, Zhao E J, Xiang H P, Hao X F, Liu X J and Meng J 2007 *Phys. Rev. B* **76** 054115
[42] Shen N F, Yang X D, Wang X X, Wang G H and Wan J G 2020 *Chem. Phys. Lett.* **749** 137430
[43] Fivaz R and Mooser E 1967 *Phys. Rev.* **163** 743
[44] Qiao J, Kong X, Hu Z X, Yang F and Ji W 2014 *Nat. Commun.* **5** 4475
[45] Radisavljevic B, Radenovic A, Brivio J, Giacometti V and Kis A 2011 *Nat. Nanotechnol.* **6** 147
[46] Tan C, Yang Q, Meng R, Liang Q, Jiang J, Sun X, Ye H and Chen X P 2016 *J. Mater. Chem. C* **4** 8171